WISC

UNIVERSITY OF WISCONSIN • MADISON, WISCONSIN

PLASMA PHYSICS

CALIBRATION TECHNIQUES FOR A FAST DUO-SPECTROMETER

J.T. Chapman
D.J. Den Hartog

DOE/ER/53198-275

June 1996

ONSIN

NOTICE

Printed in the United States of America
Available from
National Technical Information Service
U.S. Department of Commerce
5285 Port Royal Road
Springfield, VA 22161

NTIS Price codes
Printed copy: A02
Microfiche copy: A01

Calibration Techniques for a Fast Duo-Spectrometer

J. T. Chapman and D. J. Den Hartog

University of Wisconsin – Madison, Department of Physics,

1150 University Ave, Madison, WI 53706

(June 18, 1996)

Abstract

We have completed the upgrade and calibration of the Ion Dynamics Spectrometer (IDS), a high-speed Doppler duo-spectrometer which measures ion flow and temperature in the MST Reversed-field Pinch. This paper describes an *in situ* calibration of the diagnostic's phase and frequency response. A single clock was employed to generate both a digital test signal and a digitizer trigger thus avoiding frequency drift and providing a highly resolved measurement over the system bandwidth. Additionally, we review the measurement of the spectrometer instrument function and absolute intensity response. This calibration and subsequent performance demonstrate the IDS to be one of the fastest, highest throughput diagnostics of its kind. Typical measurements are presented.

52.70.Kz 07.60.Rd

I. INTRODUCTION

On the MST RFP [1] we have developed a fast passive Doppler spectrometer [2] for the study of ion dynamics. The spectrometer collects radiation from opposing directions along a toroidal chord, measuring the Doppler shift and broadening of various impurity lines with $\leq$10 μs resolution. Over its two years of operation the Ion Dynamic Spectrometer (IDS) has provided routine measurements of ion flow velocity and temperature over a variety of operating conditions. In addition the IDS has broadened our understanding of the phenomenology of fluid braking and anomalous ion heating during sawteeth events characteristic to RFP discharges [3–7]. In a recent upgrade of the diagnostic interference filters were replaced by small concave holographic grating monochrometers which have greatly improved light throughput and rejection of interfering lines. The system digitizers have also been upgraded from 100 kHz to 1 MHz along with the analog electronics to increase the analog bandwidth to 250 kHz. This will allow for more highly resolved measurements of the sudden fluid deceleration and anomalous ion heating during sawteeth events. The broad bandwidth will also facillitate the investigation of MHD activity (10-30 kHz). In particular the upgrade will allow the first direct measurement of the dynamo electric field, $\mathbf{E_d} = \langle \tilde{\mathbf{v}} \times \tilde{\mathbf{b}} \rangle$, which is believed to maintain the magnetic configuration of an RFP discharge [8]. This paper reports on the complete calibration of the upgraded system and presents data which demonstrates its upgraded capability. Particular attention is given to the system phase and frequency response which was measured *in situ* using a synchronized digitizer and signal generator. Methods to measure the IDS single channel transfer function and absolute photon response will also be described.

II. CALIBRATION

A. Phase and frequency response

We performed a highly resolved *in situ* calibration of the entire IDS system phase response from 5 to 500 kHz. Figure 1 contains a sketch of the setup used for the calibration. The Quatech WSB-100 programmable D/A board, the key component of the calibration, generates an arbitrary function with 12 bit vertical resolution and a 20 MHz clock rate. The board generates continuous wave trains by cycling through a stored sinusoidal function with an integer number of clock cycles per period. Simulations demonstrate that at frequencies with as few as 40 steps per signal cycle the driving frequency retains greater than 99% of the signal power. The generator drove a bright LED, biased to insure a linear dynamic response to the driving signal. Fiber optics collected the oscillating light signal and passed it through the full IDS system. The 32 channel output from the IDS and the LED driving signal was digitized at 1 MHz with 12 bit resolution Aurora 14 digitizers. The 20 MHz WSB-100 data strobe, divided down to 1 MHz by a simple TTL circuit, clocked the digitizers insuring strict synchronization of the driving signal and data collection.

The signal output from the jth channel of the IDS at time t_i can be modeled as

$$X_j(t_i) = S_j \sin(\omega_d t_i + \phi_j) + \delta_j(t_i), \tag{1}$$

where S_j and ϕ_j are the absolute amplitude and phase of the signal transmitted through the IDS, δ_j is a random deviate representing the photon fluctuation noise, and ω_d is the LED driving frequency. As Figure 2a depicts, the photon fluctuation noise amplitude dominates the low amplitude transmitted signal recorded at the output of the IDS. The correlation of $X_j(t)$ with a sinusoid of angle ψ at exactly $\omega_o = \omega_d$ over the full record length, L, yields the function [9],

$$C_j(\psi) = \frac{1}{L}\sum_{i=1}^{L} X_j(t_i)\sin(\omega_o t_i + \psi) = \frac{1}{2}S_j \cos(\psi - \phi_j) + \mathcal{O}\Big(\frac{\delta_{rms}}{L}\Big). \tag{2}$$

The first term on the right hand side of this equation represents the zero frequency beat wave between the correlated signals, and contains information about both the phase and amplitude

of the transmitted signal. The remaining term represents the DC beat wave between the sinusoid and the Fourier component of the noise at the pulsed frequency and is small if $L >> 1$. A linear fit to $C_j(\psi)$ through its positive-going root yields the correlation angle $\psi = \phi_j - \pi/2$ (Figure 2c). We are then able to evaluate $C(\psi = \phi_j)$, making $\cos(\psi - \phi_j) = 1$ and yielding S_j. The amplitude and phase of the reference signal, S_{ref} and ϕ_{ref}, may be obtained identically. This allows calculation of the phase lag, $\Phi_j(\omega_d) = \phi_j - \phi_{ref}$, introduced by the channel and the relative channel response amplitude, $R_j(\omega_d) = S_j/S_{ref}$.

The above analysis relies on the record length satisfying $L >> \delta_{rms}/S_j$, a condition easily satisfied by 128 K digitizer records. In addition, to retain the first term in Eq. 2, the condition $\omega_d = \omega_o$ must be precisely satisfied. Inexact knowledge of the driving frequency will introduce a non-zero beat frequency, $\omega_b = \omega_o - \omega_d$, into the correlation term causing it to vanish if L exceeds a beat period. Similarly, slight drifts in ω_d quickly decorrelate X_j and the sinusoid. If these drifts and errors are well known Eq. 2 may still be used if the record length is shortened to a fraction of the beat period and signal correlation length. However, employing the data strobe from the D/A signal generator to clock the digitizers, enables ω_d to be known *exactly* in the data regime, insuring an identically zero beat frequency and an effectively infinite correlation length.

Figure 3 shows the measured system response amplitude and phase averaged over the 32 channels. The system exhibits an extremely linear phase response from DC to 250 kHz corresponding to a nondispersive signal delay of $3.64\mu s$. The wide bandwidth of the diagnostic removes the analog electronics as the limiting factor for time resolution of physical phenomena. This limit is currently imposed either by the viewing chord which spatially averages over fast fluctuations of highly localized phenomena, or the low spectral irradiance of the impurity being observed. However, for large scale phenomena of bright impurities the IDS is capable of resolving velocity and temperature dynamics with better than $10\mu s$ resolution.

B. Instrument function

To measure the individual channel transfer functions we employed a Cadmium lamp powered by a regulated DC current source. A precision motor drive rotated the spectrometer grating sweeping the 226.5 nm Cadmium line in 5th order across the exit fiber-optic array. A single sweep of the Cadmium line traced out the instrument functions of sixteen IDS channels, corresponding to one view of the diagnostic. A photo diode detector provided a reference measurement of the lamp brightness, which varied $\sim 4\%$.

The area, centroid, and variance of each instrument function were calculated statistically, while the value and location of the instrument function maximum were estimated via a parabolic fit to the peak of each trace pulse. A linear fit to both sides of the peak provided an estimate of the instrument function FWHM. Additional sweeps for each view which included a neighboring Cadmium line at 283.7 nm in fourth order provided a conversion factor from the digitized time axis to a wavelength axis equal to the known wavelength separation of the two lines divided by their measured separation in time. Final sweeps in which both IDS views were illuminated determined the relative position of one set of sixteen channels to the other.

C. Absolute photon response

The absolute photon response of the IDS was measured using an integrating sphere with a well calibrated luminosity and blackbody spectral response. The sphere, placed directly in front of one of the two collecting lenses, illuminated 16 of the 32 IDS channels. Digitizing the 16 output signals at 1 MHz, 128K records were collected at various PMT bias voltages. The statistics of the photo-electrons emitted by the photo cathode of the PMT should dominate the statistics of the signal, y. By assuming the photo-electron emission to be a Poisson process one can realate the moments of y to the mean number of photo-electron counts per sample, $\langle n_{pe} \rangle$, and the sensitivity of our detection system to the incident photo-electrons,

G_{pe}, as:

$$\langle y \rangle = G_{pe} \langle n_{pe} \rangle \quad . \tag{3a}$$

$$\left\langle y^2 \right\rangle - \langle y \rangle^2 = G_{pe}^2 \left(\langle n_{pe}^2 \rangle - \langle n_{pe} \rangle^2 \right) = 2 G_{pe}^2 \langle n_{pe} \rangle \Delta f \, \tau_{samp}. \tag{3b}$$

Here Δf is the analog bandwidth of the diagnostic and τ_{samp} is the sampling interval of the system digitizers. Additional corrections to Eq. 3b due to PMT dark current and the single electron response pulse distribution should be of order unity [10] within the precision of this calibration. However, the calibration data exhibits an unexpected quasi-Gaussian spike in the distribution about the signal baseline in addition to the expected Poisson distribution (Figure 4a). While the dark current originating within the PMT dynode chain is too small to account for all of the spike, a possible explanation lies in the delta function response of the detection system. Digitizer sampling 1 MHz of individual PMT photoelectrons in the wings of the response which rings about zero due to the finite systme bandwidth may effectively pull a portion of the count distribution to negative and near zero values. Unfortunately, we have been unable thus far unable to reproduce this feature in simulations which incorporate these effects. A Gaussian fit to the distribution below the baseline (Figure 4b) subtracted from the whole distribution recovers a distribution which more closely approximates a Poisson curve (Figure 4c). Calculation of the moments of this distribution yields, through Eq. 3, estimates for $\langle n_{pe} \rangle$ and G_{pe}.

The photon flux incident on a single channel from the calibrated source is given by

$$\Gamma_\gamma = \frac{I_\lambda \eta_{ch} \Delta_{ch}}{\mathrm{hc}/\lambda}, \tag{4}$$

where I_λ is the spectral irradiance of the integrating sphere, η_{ch} is the system étendue per channel of $11.7 \times 10^{-5} \mathrm{sr\,cm^2}$, Δ_{ch} is the single channel width of 0.024 nm, and λ is 529.1 nm. This yields a $\Gamma_\gamma \approx 400$ photons/μs which when compared to the derived photo-electron flux, $\Gamma_{pe} = \langle n_{pe} \rangle / \tau_{sample} = 1.5\,\mathrm{p.e.}/\mu\mathrm{s}$, corresponds to a total system efficiency of 0.3%. This value agrees well with a value of 2% for the system optical transmission efficiency

estimated during the original diagnostic design multiplied by 15%, the quantum efficiency of the PMT's listed in manufacturer's specifications.

III. ANALYSIS AND RESULTS

A non-linear Gaussian fit yields the moments of the Doppler broadened line profiles output from the IDS [11]. Simulations have demonstrated that smoothing the raw data prior to conducting a fit reduces noise in the fit moments more effectively than smoothing the moments of fits to the raw data. Typically, data is binned from 1 MHz to 100 kHz prior to analysis because MHD phenomena in MST above 20 kHz is spatially averaged out. The IDS 250 kHz analog bandwidth maintains the capacity to observe fast, well-illuminated, global events.

The extremely linear phase response and broad analog bandwidth allow for the subtraction of a constant time delay from the time axis in place of a Fourier deconvolution of the system response from the raw data. Additionally, the narrowness of the single channel instrument function relative to the temperature broadened line width allow the approximation of the instrument function by a Gaussian. This enables the recovery of the thermal line width, σ_{th}, from the fit moment of the convolved profile, σ_{fit}, as,

$$\sigma_{th}^2 = \sigma_{fit}^2 - \sigma_{ch}^2, \tag{5}$$

where σ_{ch} is the variance of the single channel instrument function. For normal plasma parameters this amounts to a small correction.

Figure 5 contains flow and temperature data from a typical MST discharge which demonstrates the upgraded capabilities of the IDS. The diagnostic clearly resolves the sudden, regular braking of the plasma flow that coincides with the discrete relaxation events known as sawtooth crashes [12]. The IDS allows the accurate measurement of the $\leq 100\mu s$ deceleration on an individual sawtooth basis. These events are also characterized by the sudden spikes in the ion temperature apparent in Figure 5b. While diagnostic techniques such as

charge exchange analysis provide measurements of ion temperature they typically lack the time resolution of the IDS. The mode of operation used for this discharge is characterized by a period of small, rapid, sawtooth-like events, seen from 20 to 25 ms in Figure 5a-b. The IDS resolves the ion temperature and flow dynamics associated with these rapid events in addition to the final sawtooth crash which terminates the period and effects a dramatic reversal of the plasma flow direction at 25 ms. To facilitate presentation, the data shown in Figure 5a-b is binned at 20 kHz. However, the expanded plot of 2 ms about the sawtooth crash (Figure 5c-d) contains data points fit every $10\mu s$. Zooming in on this event it is apparent that what seemed a single braking event in Figure 5a is in fact two distinct braking events separated by less than $50\mu s$. A corresponding double spike can also be discerned in Figure 5d for the expanded temperature. This feature, invisible to resolutions $\geq 20\mu s$, could not have been observed with the IDS system prior to its upgrade

IV. SUMMARY AND DISCUSSION

The upgrade to the IDS has made it one of the fastest, highest resolution spectroscopic diagnostics of its kind. A calibration technique employing a D/A signal generator synchronized with the system digitizers provides an accurate, *in situ* measurement of the system phase and amplitude response from 5 to 500 kHz. This calibration demonstrates that the IDS has an extremely linear phase response over a 250 kHz analog bandwidth. Measurement of the single channel instrument functions was performed with a bright Cadmium line swept over the sixteen channel array. In addition an estimate of the absolute photon response using a statistical analysis of the light signal transmitted through the IDS system from a blackbody spectral source shows a system gain and transmission efficiency in agreement with previous estimates. In operation the IDS has proven a powerful and robust measurement tool of fast global ion velocity and temperature dynamics. Measurements of events with the $\leq 10\mu s$ resolution of the upgraded IDS allow the quantitative measurement of rapid changes in the equillibrium ion flow and temperature typically associated with flux generating saw-

teeth events. In addition the enchanced resolution facillitates the investigation of plasma phenomena associated with MHD fluctuations in the fluid flow previously invisible on the MST.

ACKNOWLEDGMENTS

The author would like to thank the members of the MST group for numerous discussions and to acknowledge the support of MST engineering and technical staff. This work made possible through funding from the U.S. Department of Energy.

REFERENCES

[1] R. N. Dexter, D. W. Kerst, T. W. Lovell, S. C. Prager, and J. C. Sprott, Fusion Technol. **19**, 131 (1991).

[2] D. J. Den Hartog and R. J. Fonck, Rev. Sci. Instrum. **65**, 3238 (1994).

[3] D. J. Den Hartog, A. F. Almagri, J. T. Chapman, R. J. Fonck, C. C. Hegna, H. Ji, S. C. Prager, and J. S. Sarff, Phys. Plasmas **2**, 2281 (1995).

[4] S. C. Prager, A. F. Almagri, M. Cekic, J. T. Chapman, D. J. Den Hartog, G. Fiksel, C. C. Hegna, H. Ji, and J. S. Sarff; J. R. Drake, S. Mazur, P. Nordlund, and H. E. Saetherblom, Plasma Phys. and Contr. Fusion **37**, A303 (1995).

[5] A. F. Almagri, J. T. Chapman, C. S. Chiang, D. J. Den Hartog, K. A. Mirus, S. C. Prager, and J. S. Sarff, Bull. Am. Phys. Soc. **40**, 1753 (1995).

[6] D. J. Den Hartog, A. F. Almagri, J. T. Chapman, A. K. Hansen, C. C. Hegna, S. C. Prager, and J. S. Sarff, Bull. Am. Phys. Soc. **40**, 1753 (1995).

[7] M. Yokoyama, J. D. Callen and C. C. Hegna, "Evolution of Toroidal Flow During, After Mode Locking", University of Wisconsin Center for Plasma Theory and Computation Report, UW-CPTC 95-4 (1995).

[8] S. Ortlani and D. D. Schnack, *Magnetohydrodynamics of Plasma Relaxation*, World Scientific, Singapore, 1993.

[9] J. S. Bendat and A. G. Piersol, *Engineering Applications of Correlation and Spectral Analysis*, John Wiley and Sons, New York, 1980.

[10] Thorn EMI Electron Tubes, "photomultimpliers and accessories", 1993.

[11] D. J. Den Hartog, A. F. Almagri, and S. C. Prager, Rev. Sci. Instrum. **66**, 444 (1995).

[12] S. Hokin, A. Almagri, S. Assadi, J. Beckstead, G. Chartas, N. Crocker, M. Cudzinovic, D. Den Hartog, R. Dexter, D. Holly, S. Prager, T. Rempel, J. Sarff, E. Scime, W. Shen,

C. Spragins, C. Sprott, G. Starr, M. Stoneking, and C. Watts, Phys. Fluids B **3**, 2241 (1991).

FIGURES

FIG. 1. Schematic of the *in situ* calibration of the IDS response amplitude and phase. The Quatech WSB-100 provides the clock for both the driving signal and the Aurora 14 digitizers.

FIG. 2. Extraction of phase information from noisy IDS output signals using correlation analysis. a) An oscillating signal, S_{ref}, drove an LED at ω_d. The digitized data points are represented above with closed circles. b) The signal output from the jth channel, X_j, contains both the phase lagged output signal, S_j, and photon noise fluctuations with amplitude δ_{rms}, recorded at the closed squares. c) Correlation of the driving signal and X_j with a sinusoid at exactly $\omega_o = \omega_d$ over 2π yields the correlation function $C_{ref}(\psi)$ and $C_j(\psi)$ respectively. The phase lag introduced by the channel, $\Phi_j(\omega_d)$, is retrieved as the angle between the two positive going roots of the correlation functions. The relative channel response is calculated as, $R_j(w) = S_j/S_{ref}$.

FIG. 3. The calibrated phase and amplitude response from 5-500 kHz is shown averaged over the 32 IDS channels. The sytem response amplitude (solid) drops 5 dB from 5 to 250 kHz providing a broad analog bandwidth. From 250-500 kHz the response drops to -24 dB insuring negligible aliasing of high frequency noise. The system phase response (dashed) is exceptionally linear over the effective analog bandwidth corresponding to a nondispersive signal delay of $3.64\mu s$.

FIG. 4. a) A histogram of digitized signal level yields a curve which appears to be a super position of the expected Poisson curve with a Gaussian spike about the channel baseline. b) A fit to the distribution below the baseline reveals an approximately Gaussian shape. c) Subtraction of the fitted Gaussian from the distribution recovers a distribution above the baseline which more closely approximates a Poisson curve. Here the horizontal axis has been renormalized to the corresponding number of incident photoelectrons and the Poisson curve corresponding to the calculated signal mean and variance is over drawn.

FIG. 5. IDS data from a typical MST discharge. a) The IDS resolves sharp decelerations in the ion flow during sawteeth events at 8, 13, 25, and 32 ms. b) These braking events are typically accompanied by large, sudden spikes in the ion temperature over which the impurity line profile remains thermal. c) Expanding the data about the large sawtooth at 25 ms reveals two distinct braking events separated by less than $50\,\mu s$. d) The corresponding heating spikes can also be discerned in the expanded temperature data.

Fig 1

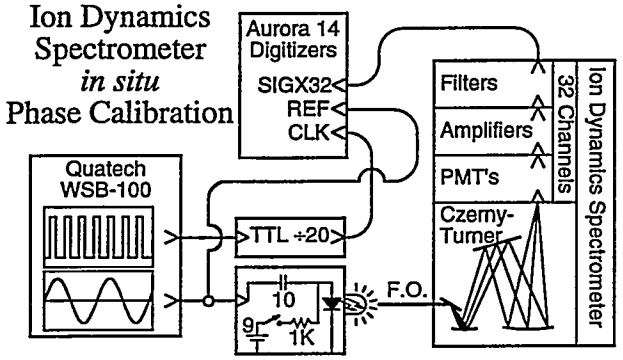

Fig 2

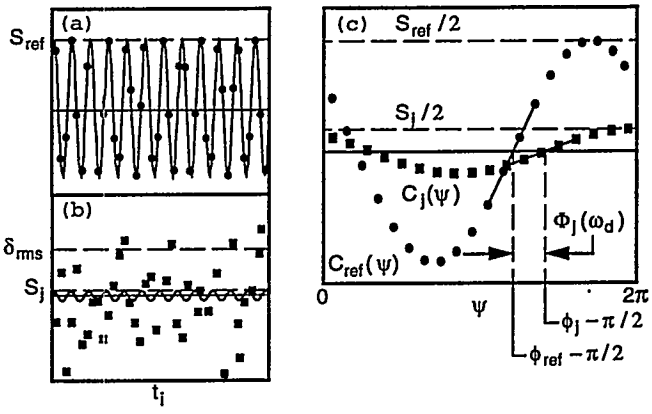

Fig 3

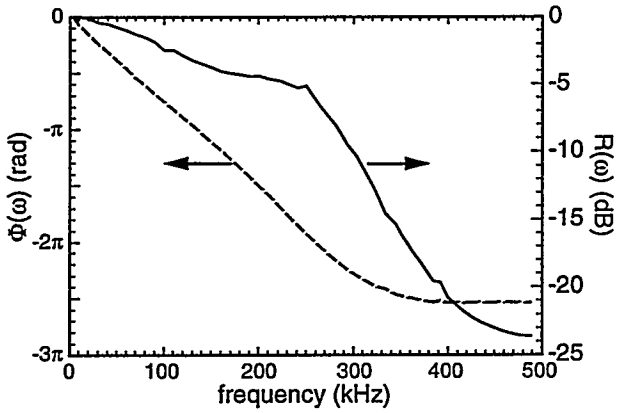

Fig 4

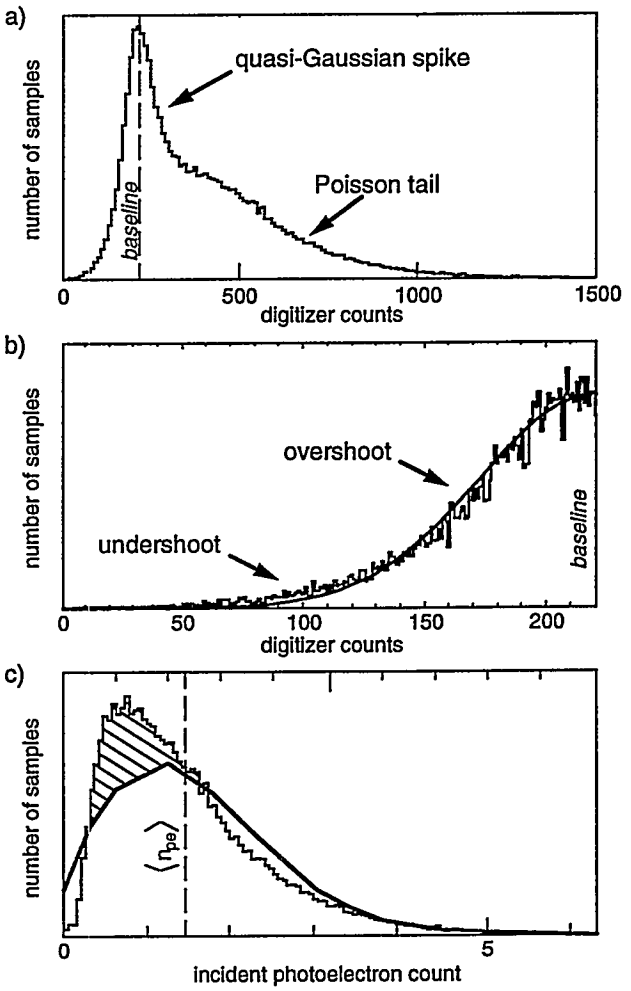

Fig 5

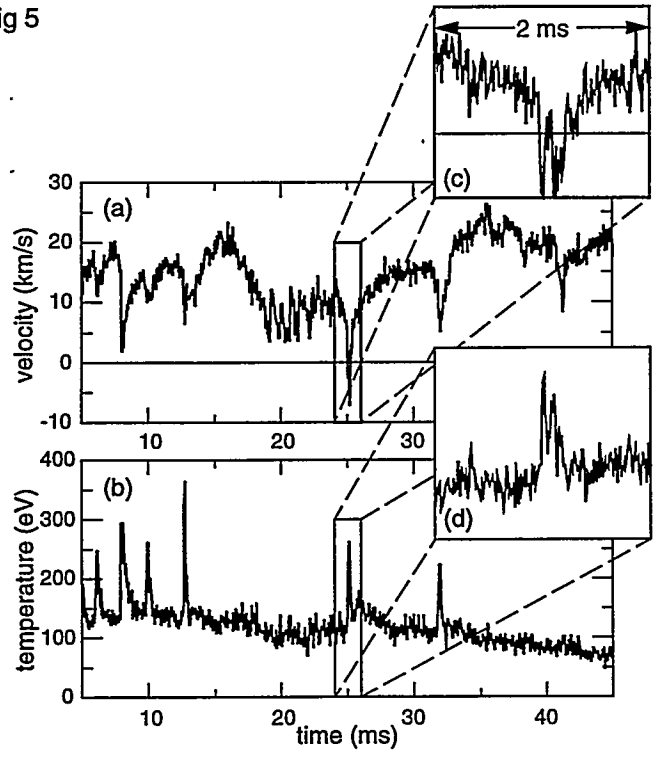

RED COVER REPORT APPENDIX

This appendix contains specific results from the IDS calibration. The methods employed to achieve these results are detailed in the preceding paper.

FIG. A1. The measured instrument functions from three adjacent channels exhibit a roughly triangular shape. The channels overlap at half max corresponding to an optimal compromise between spectral luminosity and resolution.

FIG. A2. Each view of the IDS covers slightly less than 4 Å of the spectrum in 0.25 Å steps. Channel position was estimated via a parabolic fit to the top of the individual channel instrument functions.

FIG. A3. The channel to channel normalization exhibits little dependence on PMT bias setting. Comparison with a similar calibration performed one year prior to the current results shows little drift in relative channel sensitivity over time.

FIG. A4. The FWHM of each channel was estimated with a linear fit to the sides of the instrument function. The channels are approximately a quarter of an Angstrom wide. Error estimates are derived from the statistical fluctuations among four separate measurements.

FIG. A5. The channel variance was calculated statistically from the instrument functions. The average instrumental variance of each view is subtracted in quadrature from the measured variance of the thermally broadened line during data analysis. This instrumental contribution to line width is important only for very cold plasmas.

FIG. A6. A 3052 K blackbody curve provides an excellent fit to the integrating sphere calibration data provided by the sphere manufacturer. The curve provided an estimate of the sphere luminosity at the observed wavelength of 529.05 nm.

FIG. A7. a) The amplitude of the anomalous quasi-Gaussian spike about zero increased as the PMT bias was decreased. b) However the variance of the spike increased with PMT bias. Thus, as the PMT bias was increased the spike shortened and broadened. These effects have not been reproduced in simulations.

FIG. A8. a) The calculated gain of the system (digitizer counts/photon-μs) increases as would be expected with PMT bias. b) The estimated incident photo-electron flux remains constant for each of the PMT settings. This is consistent with our light source maintaining constant luminosity throughout the calibration.

Fig A1

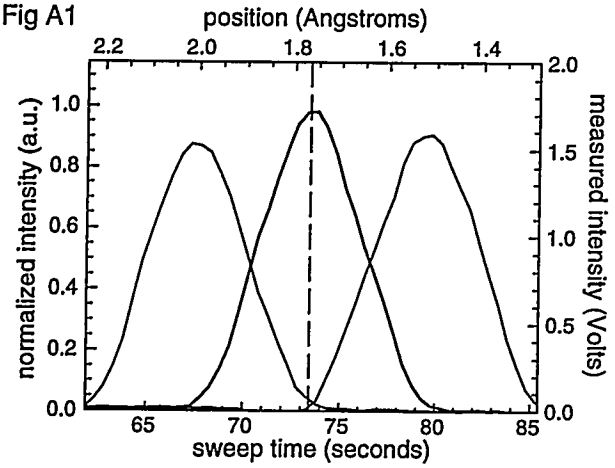

Fig A2

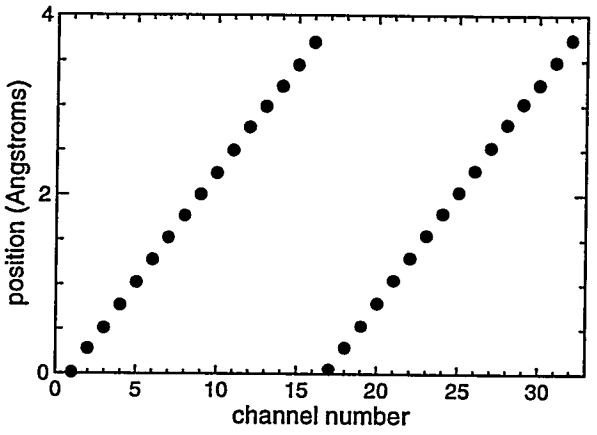

Fig A3

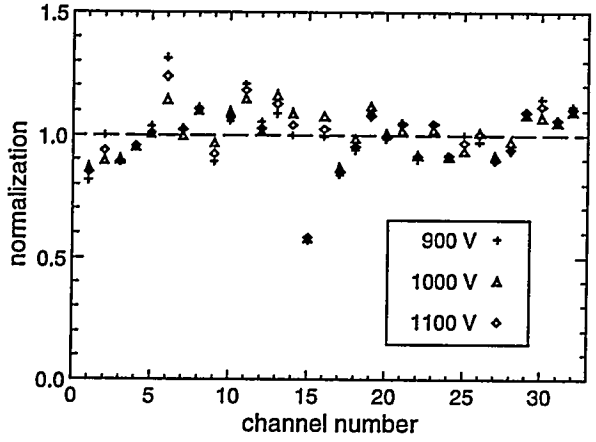

Fig A4

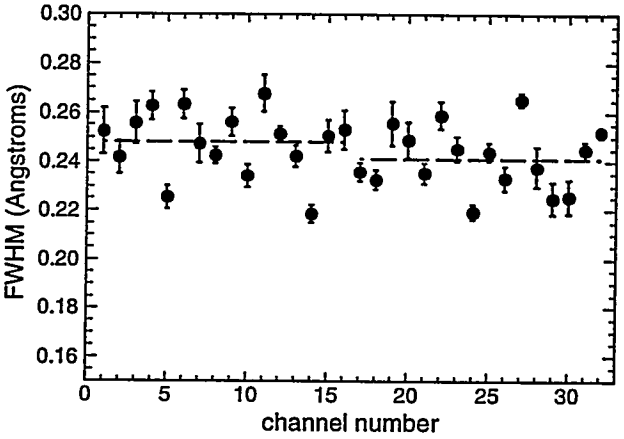

Fig A5

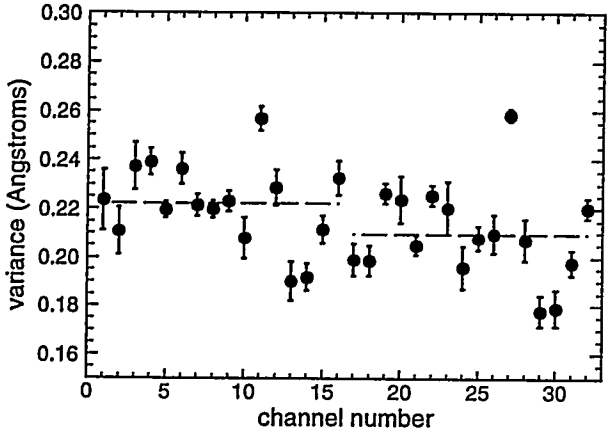

Fig A6

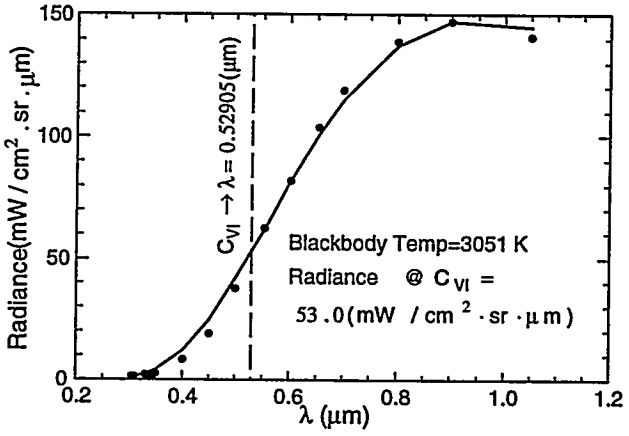

Fig A7

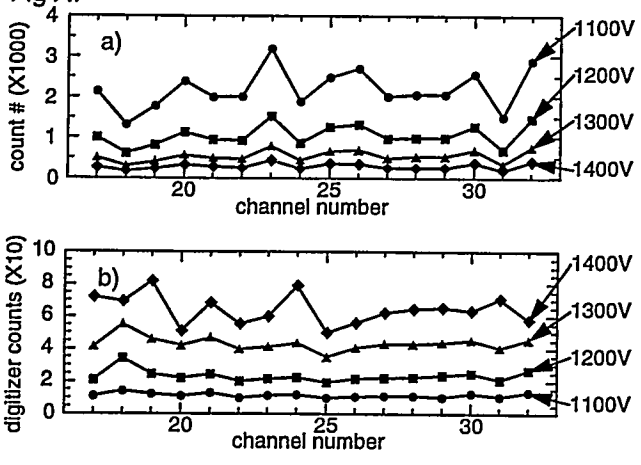

Fig A8

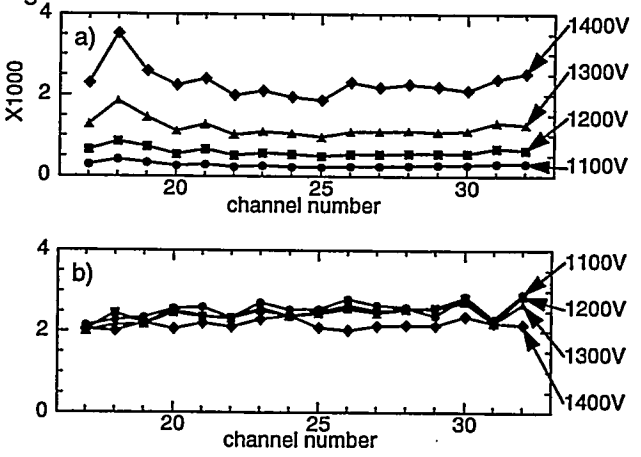

EXTERNAL DISTRIBUTION IN ADDITION TO UC-20

S.N. Rasband, Brigham Young University
R.A. Moyer, General Atomics
J.B. Taylor, Institute for Fusion Studies, The University of Texas at Austin
E. Uchimoto, University of Montana
F.W. Perkins, PPPL
O. Ishihara, Texas Technical University
M.A. Abdou, University of California, Los Angeles
R.W. Conn, University of California, Los Angeles
P.E. Vandenplas, Association Euratom-Etat Belge, Belgium
Centro Brasileiro de Pesquisas Firicas, Brazil
P. Sakanaka, Institute de Fisica-Unicamp, Brazil
Mme. Monique Bex, GANIL, France
J. Radet, CEN/CADARACHE, France
University of Ioannina, Greece
R. Andreani, Associazione EURATOM-ENEA sulla Fusione, Italy
Biblioteca, Istituto Gas Ionizzati, EURATON-ENEA-CNR Association, Italy
Plasma section, Energy Fundamentals Division Electrotechnical Laboratory, Japan
Y. Kondoh, Gunma University, Kiryu, Gunma, Japan
H. Toyama, University of Tokyo, Japan
Z. Yoshida. University of Tokyo, Japan
FOM-Instituut voor Plasmafysica "Rijnhuizen," The Netherlands
Z. Ning, Academia Sinica, Peoples Republic of China
P. Yang, Shandong University, Peoples Republic of China
S. Zhu, University of Science & Technology of China, People's Republic of China
I.N. Bogatu, Institute of Atomic Physics, Romania
M.J. Alport, University of Natal, Durban, South Africa
R. Storer, The Flinders University of South Australia, South Australia
B. Lehnert, Royal Institute of Technology, Sweden
Librarian, CRPP, Ecole Polytechnique Federale de Lausanne, Switzerland
B. Alper, Culham Laboratory, UK
A. Newton, UK

2 for Chicago Operations Office
5 for individuals in Washington Offices

INTERNAL DISTRIBUTION IN ADDITION TO UC-20
80 for local group and file